

Adapting Self-Supervised Learning for Computational Pathology

Eric Zimmermann¹, Neil Tenenholtz¹, James Hall¹, George Shaikovski², Michal Zelechowski², Adam Casson², Fausto Milletari², Julian Viret², Eugene Vorontsov², Siqi Liu², and Kristen Severson^{1,†}

¹Microsoft Research, Cambridge, MA United States

²Paige, NYC, NY United States

Abstract

Self-supervised learning (SSL) has emerged as a key technique for training networks that can generalize well to diverse tasks without task-specific supervision. This property makes SSL desirable for computational pathology, the study of digitized images of tissues, as there are many target applications and often limited labeled training samples. However, SSL algorithms and models have been primarily developed in the field of natural images and whether their performance can be improved by adaptation to particular domains remains an open question. In this work, we present an investigation of modifications to SSL for pathology data, specifically focusing on the DINOv2 algorithm. We propose alternative augmentations, regularization functions, and position encodings motivated by the characteristics of pathology images. We evaluate the impact of these changes on several benchmarks to demonstrate the value of tailored approaches.

1. Introduction

Pathology is the study of the causes and effects of disease and is used as a foundation for diagnosis and treatment. Pathology relies on the study of stained tissue microscopy slides, also known as whole slide images (WSIs). Computational pathology (CPath) refers to the application of artificial intelligence to WSIs which have been digitized enabling automated study and characterization [13, 14, 28, 29]. Several factors have recently converged to drive increased interest in the use of foundation models, large-scale deep neural networks trained on expansive datasets without access to task-specific labels, in CPath. Foundation models have demonstrated incredible success in the natural image domain, even in cases with limited labeled data

for training, by learning image representations, called embeddings, which can be used as inputs to a wide-variety of downstream tasks. These properties are desirable for the pathology domain as there are many tasks, such as diagnosis, disease subtyping, biomarker quantification, estimation of treatment response, and survival prediction, and curated labeled datasets are expensive to gather as they require expert review. Motivated by these factors, there have been recent efforts to collect large pathology image datasets and subsequently several foundation models have been proposed [2, 9, 12, 15, 17, 23, 32, 34].

The rise of foundation models has been enabled in part by the use of self-supervised learning approaches. Self-supervision is a learning paradigm where a pre-text task is constructed without access to target labels. The quality of features learned and their ability to transfer to a target task is highly dependent on the definition of the pre-text task and its correlation to downstream objectives. Joint-embedding self-supervised learning (JE-SSL) methods pose the learning objective in terms of alignment and diversity [6, 33]. Alignment is accomplished by encouraging the embeddings of pairs or sets of samples generated from the same source image via the application of an augmentation policy to be close to one another [4, 10, 37]. Diversity provides the necessary support to learn representation that avoid collapse or trivial solutions across the entire set of observations. Examples of diversity objectives include using explicit constraints such as decorrelation, maximum entropy, and minimum energy as well as implicit constraints such as model asymmetry or centering operations [8, 11, 18, 33].

The choice of augmentation policy is a key factor in determining what kinds of features may be learned during training. Often, augmentation strategies designed for natural images are directly applied to other domains, as has largely been the case in computational pathology. However it is unclear that the same augmentations will produce good features across domains. Indeed it has been shown that the effects of augmentation are often data dependent and vary

[‡]Presented at DCA in MI Workshop, CVPR 2024

[†]Corresponding author: kseverson@microsoft.com

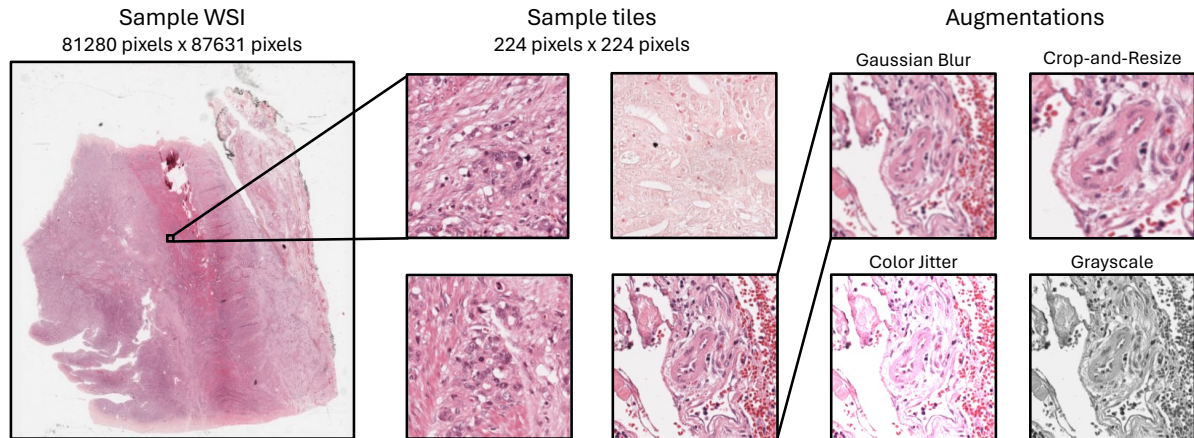


Figure 1. Example of a computation pathology data pipeline for self-supervised learning. Tiles (center) that satisfy a tissue inclusion criteria are randomly sampled from a WSI (left) and perturbed using a set of augmentations sampled from a policy to build the self-supervised pre-text task (right). Augmentations include but are not limited to Gaussian blur, color jitter, grayscale, and crop-and-resize.

across classes [3]. Unlike natural images, which are a 2D projection of a 3D scene, CPath images are acquired from essentially 2D slices of tissue that are stained and scanned at various resolutions or magnifications through a digitization process. One implication of this is that pixels have a known corresponding physical distance. Understanding the relative distances and shapes of morphological features may be instructive when interpreting the image. A further distinction of pathology data as compared to natural images is that tissue patterns are non-unique and less diverse across a population. These facts motivate the investigation of changes to standard self-supervised learning strategies.

In this work, we investigate the use of domain-inspired modifications to self-supervised learning algorithms and the ViT architecture focusing on preserving and accounting for morphological patterns. We choose DINOv2 [25], a self-supervised distillation method, as the framework to test the impact of different design choices and evaluate performance on various benchmark tasks. Our results indicate that preserving local morphology and modifying regularization schemes lead to better performance.

2. Related Work

Possibly in part due to the computational cost, few works have studied the impact of augmentation policies in CPath foundation models on downstream task performance, however there are a few notable exceptions. Tellez et al. [30], Ciga et al. [12], and Gullapally et al. [19] all investigated the impact of color augmentation motivated by stain variation, the effect of differences in staining protocol and scanner type which do not reflect underlying differences in pathology. All of the aforementioned studies have demonstrated improvements in performance using color augmen-

tation and several models have employed domain-orientated approaches [15, 34]. Digitized WSIs are typically stored at fixed magnifications, e.g. $5\times$, $10\times$, $20\times$, and have significantly less variability in object scale than natural images. As noted in the introduction, this feature also draws into question augmentation protocols that typically crop and resize images. In addition to color variation, Ciga et al. [12] investigated the impact of random cropping on model performance and found less random cropping generally improved performance although the largest observed improvement in any setting was 5%.

3. Learning on gigapixel pathology images

WSIs are gigapixel images, typically tens of thousands of pixels in each spatial dimension. In order to avoid the computational bottlenecks associated with large images, foundation models have been trained using local regions of the image called tiles (see Fig.1). Tiles are extracted by subdividing an image into non-overlapping regions that have sufficient amounts of relevant tissue as determined by a separate inclusion criterion such as a segmentation network. To-date, most works have generated tiles at a fixed magnification, typically $20\times$. As pathology features manifest at various resolutions, we instead consider a set-up where tiles are drawn from the most commonly available magnifications, $5\times$, $10\times$, $20\times$, and $40\times$, or 2.0, 1.0, 0.5 and 0.25 microns-per-pixel, respectively.

Given this setup, in the next two sections, we discuss how pairwise alignment tasks and diversity objectives can be adapted to be more suited to pathology image features. We focus our description to the DINOv2 algorithm [25] and vision transformer architectures [16]. The DINOv2 approach uses self-distillation cross-entropy, masked image

modeling, and differential entropy to learn image features. It has recently been used to train several CPath foundation models [9, 15, 23, 32] and we therefore use it to frame our analysis, however we expect that many of the insights can generalize to other self-supervised learning settings.

3.1. Morphology-preserving alignment

The alignment component of JE-SSL objectives is achieved via an invariance objective that is controlled through a careful selection of an augmentation policy. The augmentation policy is applied as follows: for a sample x drawn from a dataset \mathcal{D} , T random perturbations are sampled from the augmentation policy \mathcal{T} and applied to create views $\{\mathcal{T}_t(x)\}_{t=1}^T$. These views then serve as input to the alignment objective. Examples of common augmentations are shown in Fig. 1.

The design of the augmentation policy determines the properties of the network and must be difficult enough to learn meaningful information without shortcuts. Traditional augmentation policies were designed for object-centric natural images which have common reoccurring structure and texture. Color perturbation and random crop-and-resize are the fundamental building blocks of these policies and aim to decouple global-local features. The motivation for crop-and-resize is the creation of feature co-occurrences resulting from overlaps between views which can then be used for alignment [20, 22].

Cell morphology plays an important role in understanding tissue structure and disease. Depending on the aspect ratio of the crop, a resize may introduce unwanted distortions that affect tissue and cell shapes. One unique aspect of pathology data is that the training samples are constructed from tiles at predetermined sizes from a WSI. The selection of tile size is primarily unrelated to the modeling task, as it is motivated by compute constraints. Because of this, it is possible to design a translation-like augmentation that uses a larger source field of view to minimize distortions while maintaining the same output size and expected overlap of views. This operation differs from regular translations as it does not introduce imaging artifacts along boundaries, i.e. padded values. To demonstrate how this is possible, consider replacing the $L \times L$ -sized training tile with an $N \times N$ -sized source region and a target $L \times L$ tile to be sub-sampled within the larger window, where $N > L$ (see Fig. 2). This alternative augmentation, which we refer to as extended-context translation (ECT), maintains the average overlap between views as compared to the crop-and-resize method with minimal need for resizing. The particular value for N can be selected based on the desired intersection over union of views. ECT can serve as a drop-in replacement for traditional crop-and-resize approaches and can be combined with other augmentations such as color augmentations.

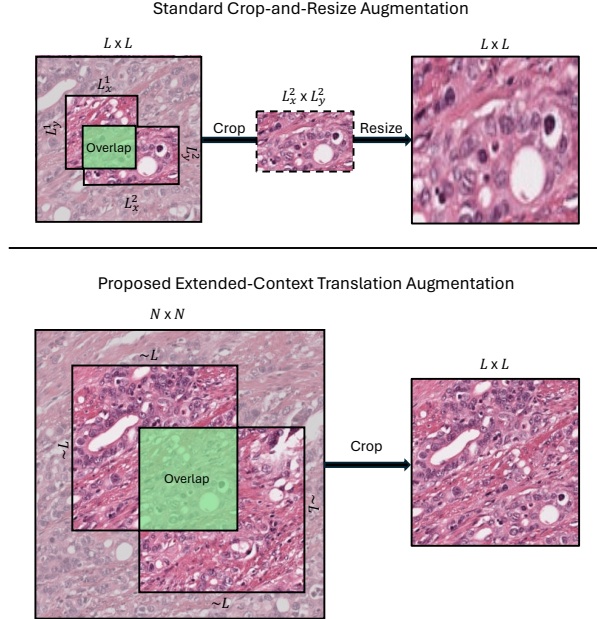


Figure 2. Illustration of crop-and-resize (top) and modified extended-context translation augmentation strategy (bottom). Crop-and-resize randomly selects a sub-region smaller than the target size and up-samples to meet the criterion. Extended-context translation extends the context window and randomly selects a sub-region that is approximately the target size.

3.2. Accounting for data redundancy

The second piece of an JE-SSL objective is a diversity function to prevent collapse of the representations. Some JE-SSL methods, like DINOv2, achieve diversity across embeddings by maximizing entropy. Although diversity objectives often share similar optimum, their dynamics throughout training are considerably different and introduce practical challenges that must be addressed.

Feature diversity is dependent on the data distribution used to train a network. In CPath, tissue patterns are repetitive across populations and as a result, the likelihood of a collision may be higher than those encountered in large uncurated natural imaging datasets. Based on the latter, estimators should be constructed under the assumption that features are not independent, may be very close together, and cannot be arbitrarily separated.

DINOv2 proposes the use of KoLeo, a differential entropy estimator defined as

$$H_{\text{KoLeo}}(f) = \frac{1}{n} \sum_{i=1}^n \min_{j \neq i} \log d(z_i, z_j), \quad (1)$$

where i indexes the samples in a batch, d is a distance measure and z is an embedding normalized to the hypersphere [27]. The inclusion of maximization of entropy using KoLeo aims to spread out learned embeddings via a

convex regularizer and has been shown to improve image retrieval performance [25]. However, when two samples are very similar, and distance approaches zero, KoLeo approaches infinity.

A kernel density estimator (KDE) can be used as an effective replacement in order to mitigate the issues associated with KoLeo in a setting where features may be clustered. The kernel entropy estimator is defined as

$$H_{\text{KDE}}(f) = -\frac{1}{n} \sum_{i=1}^n \log \sum_{j \neq i}^n k(\mathbf{z}_i, \mathbf{z}_j), \quad (2)$$

where k is an appropriate kernel function and all other terms are as defined above. Similar objectives have been used in various other methods [33, 36].

The kernel density estimator has different regularization effects for local behaviors, i.e. for samples with large and small distances, but maintains the population effect of promoting diversity. Examples of kernels include Gaussian, von Mises-Fischer (vMF), inverse multiquaratic, or Laplacian kernel each of which allows for different repulsion characteristics that have bounded gradients which can also vanish for a given pair.

3.3. Conditioning on magnification

Although not exclusively related to self-supervised learning approaches, we present an additional modeling consideration that is enabled by representations that preserve morphology. For a vision transformer (ViT) architecture [16], preserving relative distances on data that has known natural resolution hierarchies allows for additional knowledge to be embedded through a scale-aware definition of the position encodings. Scale-MAE [26], a technique developed in the remote sensing literature for geospatial data, proposes one such definition based on the Ground Sample Distance (GSD). Analogously, we propose Cell Sample Distance (CSD) position encodings

$$\begin{aligned} \mathbf{v}_{\text{csd},x}(p, 2i) &= \sin\left(\frac{m}{M} \cdot \frac{p}{\Omega^{\frac{2i}{D}}}\right), \\ \mathbf{v}_{\text{csd},y}(p, 2i + 1) &= \cos\left(\frac{m}{M} \cdot \frac{p}{\Omega^{\frac{2i}{D}}}\right), \end{aligned} \quad (3)$$

where m is encoded relative to a reference M in microns, p is the 2D position in the sequence, D is the dimension of the encoding vector, and Ω is a large constant used to modulate frequencies. This definition of position encoding can replace the more standard learned position encodings in the ViT architecture. CSD position encodings can also be used in settings with varying sequence lengths, for instance as occurs when generating global and local views, by using the known cell distance.

An alternative approach for accounting for differences in relative position as a function of magnification is to learn

position embeddings for each magnification (referred to as Learned Per Micron, or LPM, here). This approach requires pre-defining the set of magnifications of interest and cannot be dynamically adjusted.

4. Experiments

We propose a set of experiments to investigate the impact of replacing crop-and-resize with extended-context translation augmentations, KoLeo with KDE regularization, and learned position encodings with cell sample distance or learned per magnification position encodings and combinations thereof. The details of these experiments are described in the following sections.

4.1. Pretraining methodology

We select a ViT-B/16 and pretrain using DINOv2 [25]. The default parameters as described in [25] are used with the following changes: batch size of 1024, learning rate equal to $2e - 4$, and a drop-rate of 0.4. The model is trained for approximately 112K iterations, or equivalently 115M tiles, using 16 GPUs. In all experiments, grayscale, color jitter, flips, and solarization perturbations are unchanged. Crop-and-resize experiments use the DINOv2 ranges of (0.32, 1.0) and (0.05, 0.32) for global and local views with an aspect ratio range of (0.75, 1.33). ECT augmentations use a source context window of 392×392 , a scale range of (0.9, 1.1) and aspect ratio range of (0.95, 1.05). Additional implementation details are described in Appendix A. This source size was selected based on a Monte Carlo simulation to calculate the intersection-over-union for various context sizes and selecting one with similar overlap to the DINOv2 crop-and-resize overlap for 224×224 tiles. The augmentation is implemented using the same crop-and-resize module where the new scale parameters are adjusted using the relative ratio of the source and target size for both global and local views. Density estimation is computed using a vMF kernel

$$k_{\text{vMF}}(\mathbf{x}, \mathbf{y}) = \exp(\kappa \mathbf{x}^\top \mathbf{y}), \quad (4)$$

where κ is a scaling constant and is set to 5 for all experiments based on empirical results in the literature. The vMF kernel is selected because of its favorable computational qualities and its demonstrated success in encouraging diverse embeddings [7, 33]. For all CSD position encoding experiments, $\Omega = 10000$ as is done in scale-MAE [26]. All evaluation is performed using teacher predictions.

4.2. Pretraining dataset

The training dataset is comprised of 1,488,550 WSIs from 119,629 patients from Memorial Sloan Kettering Cancer Center. All WSIs are stained using hematoxylin and eosin, a routine stain. WSIs are scanned at, a possible subset of,

5 \times , 10 \times , 20 \times and 40 \times , or 2, 1, 0.5 and 0.25 microns-per-pixel, respectively. Data is pre-processed into non-overlapping 224×224 or 392×392 tiles contained at least 45% tissue coverage as determined by a hue, saturation, and value (HSV) filter with an acceptance criterion in ranges [90, 180], [8, 255], [103, 255].

4.3. Evaluation tasks

A mix of seven in-domain and out-of-domain tile level classification tasks across various magnifications are used to evaluate the quality and separability of the learned features of the teacher network via linear probe protocol. The classifier is trained on frozen embeddings generated from non-augmented model inputs for 12.5K iterations using a cosine schedule with stochastic gradient descent.

PanMSK $XX\times$ is an in-domain cancer detection task performed at 5 \times , 10 \times , and 20 \times magnifications. 1,196,171 224×224 pixel tile samples, sourced from 3,999 WSI representing 17 tissue types, are labeled either cancer or benign [32].

PCAM is a public dataset of 327,680 lymph node images labeled as cancer or benign [5, 31]. Images are up-sampled from 96×96 at 10 \times magnification to 224×224 for analysis.

MHIST is a public dataset of 3152 colorectal polyp images (5 \times magnification 224×224 pixels) labeled benign or precursor [35].

CRC is a public dataset of 100,000 colorectal images (20 \times magnification 224×224 pixels) classified into 9 morphologies [24].

MIDOG is a public dataset of 21,806 mitotic and non-mitotic events labeled on $503 \text{ } 7K \times 5K$ WSI regions from several tumor, species, and scanner types at 40 \times magnification [1]. Data was converted into a binary classification task by expanding each 50×50 pixel annotation to 224×224 regions and then randomly shifting in the horizontal and vertical regions such that the event is not centered in the tile. All negative instances that overlapped with positive instances were removed from the dataset.

5. Results and Discussion

Table 1 presents the results. Overall, the combination of ECT, standard learned position encoding, and KDE regularization performed the best, having the highest performance as measured by test accuracy on five out of seven tasks and the highest mean accuracy. The combination of cell sample distance position encoding, ECT and KDE regularization was a close second, with a mean accuracy only 0.23 less than the best result and the best performance on two of the seven tasks. Observing pairwise impacts of each setting, the change from KoLeo to KDE regularization had the largest impact (average improvement 3.52, range 1.18-5.63). ECT as opposed to crop-and-resize also improved performance in all settings on average (average improvement 0.89, range

0.18-1.61). Focusing only on the in-domain PanMSK tasks, these improvements are even more pronounced (average improvement 3.87, range 1.46-6.02 and average improvement 1.28, range 0.72-1.84 for KDE regularization and ECT, respectively). Learning position encodings per magnification did not improve performance. The combination of learned position encodings per magnification with ECT augmentation and KoLeo regularization had the worst performance overall and a mean accuracy 6.12 less than the best result.

Self-supervised pipelines are built to enforce invariance, however, equivariance may be of equal importance. Decoupling the benefits between invariance and equivariance is difficult due to the wide range of downstream tasks that are used to evaluate performance. For example, invariance to pose, color, and relative intensity will aid in generalizing across data sources given that different institutions have different slide preparation techniques and scanners [23]. Models do not necessarily utilize the same types of imaging features as a pathologist. As a result, it is unclear if being invariant or equivariant to cell shape and size through either a crop-and-resize or an extended-context translation is important. There is a trade-off that must be considered, where invariance to shape may help generalize across data sources and domains, while equivariance may lead to better in-domain features. We empirically observe, when evaluating the effect of extended-context translations, more improvement is observed for in-domain PanMSK evaluation tasks as compared to the out-of-domain tasks, on average. This result is of particular interest, since it demonstrates the benefits of preserving morphology in isolation of other confounding variables. We expect out-of-domain generalization can be further improved through additional scale, data curation, color augmentations, and training horizons. Validating this hypothesis is beyond the scope of this work.

The impact of different regularization approaches benefits from contextualization of the particular implementation details. DINOv2 implements KoLeo without synchronization across devices which couples compute configurations to performance, since the likelihood of encountering nearby pairs is proportional to the number of observations in a batch. The proposed alternative using KDE accounts for these limitations by removing instabilities through the selection of the vMF kernel, whose gradients are non-convex and vanish in a regime that would otherwise be problematic. Regardless of the potential benefits introduced from data augmentation or architecture design, if the amount of regularization is too high or improperly specified, the model’s ability to learn will be limited.

Scale-aware position encodings are well suited for reconstruction objectives like the masked autoencoder [21] as the decoder removes the need for a diversity objective and does not require strong augmentation policies such as the

Image Augmentation	Crop		Extended-Context Translation					
Position Encoding	Learned		Learned		LPM		CSD	
Regularizer	KoLeo	KDE	KoLeo	KDE	KoLeo	KDE	KoLeo	KDE
PanMSK 5x	88.96	90.05	89.89	92.17	83.82	90.66	83.85	<i>91.78</i>
PanMSK 10x	88.83	90.15	89.48	92.05	85.30	90.57	85.70	<i>91.30</i>
PanMSK 20x	85.98	87.96	86.57	<i>89.41</i>	83.63	87.84	85.14	89.66
PCAM	83.42	84.20	84.94	86.77	78.45	84.58	81.45	<i>86.64</i>
CRC	93.93	<i>94.89</i>	93.33	95.39	92.13	94.01	93.12	94.15
MHIST	79.12	77.58	76.56	<i>80.25</i>	75.33	<i>80.55</i>	72.88	81.78
MIDOG	62.86	<i>66.52</i>	63.55	66.57	61.13	64.10	59.42	65.67
Average	83.30	84.48	83.47	86.09	79.97	84.62	80.22	85.85

Table 1. Test accuracy results for seven evaluation tasks and eight model settings. In-domain evaluation tasks include PanMSK XX, while out-of-domain tasks include PCAM, CRC, MHIST, and MIDOG. Boldface indicates the best performance and italics indicates the second best performance. In a majority of tasks and on average, learned position encodings using ECT and KDE regularization performs best.

random resized crop. Unfortunately, masked autoencoders require additional finetuning to perform well on downstream tasks and are not evaluated in this study [21]. The morphology modification suggested in Sec. 3.1 preserves spatial features and unlocks the ability to explore spatial-conditioning in a joint-embedding environment. While CSD position encodings did not degrade performance, they did not provide any additional benefits. It is possible that using the position encoding in the projector, as would be more similar to the Scale-MAE setting, could lead to greater improvements in performance but that investigation is left for future work.

Overall, our results demonstrate that the incorporation of domain-specific data considerations has the ability to unlock major improvements for self-supervised CPath models. Finally we note we designed our experiments to highlight the relative impact of modeling decisions, not to compete with existing foundation model performance. In the future, we aim to understand the impacts of these modeling choices for large-scale foundation models.

References

- [1] Marc Aubreville, Frauke Wilm, Nikolas Stathonikos, Katharina Breininger, Taryn A Donovan, Samir Jabari, Mitko Veta, Jonathan Ganz, Jonas Ammeling, Paul J van Diest, et al. A comprehensive multi-domain dataset for mitotic figure detection. *Scientific Data*, 10(1):484, 2023. 5
- [2] Shekoofeh Azizi, Laura Culp, Jan Freyberg, Basil Mustafa, Sebastien Baur, Simon Kornblith, Ting Chen, Nenad Tomasev, Jovana Mitrović, Patricia Strachan, et al. Robust and data-efficient generalization of self-supervised machine learning for diagnostic imaging. *Nature Biomedical Engineering*, 7(6):756–779, 2023. 1
- [3] Randall Balestriero, Leon Bottou, and Yann LeCun. The effects of regularization and data augmentation are class dependent, 2022. 2
- [4] Adrien Bardes, Jean Ponce, and Yann LeCun. Vi-creg: Variance-invariance-covariance regularization for self-supervised learning, 2022. 1
- [5] Babak Ehteshami Bejnordi, Mitko Veta, Paul Johannes Van Diest, Bram Van Ginneken, Nico Karssemeijer, Geert Litjens, Jeroen AWM Van Der Laak, Meyke Hermsen, Quirine F Manson, Maschenka Balkenhol, et al. Diagnostic assessment of deep learning algorithms for detection of lymph node metastases in women with breast cancer. *Jama*, 318(22):2199–2210, 2017. 5
- [6] Florian Bordes, Randall Balestriero, and Pascal Vincent. Towards democratizing joint-embedding self-supervised learning, 2023. 1
- [7] Sergiy V. Borodachov, Douglas P. Hardin, and Edward B. Saff. Discrete energy on rectifiable sets. *Springer Monographs in Mathematics*, 2019. 4
- [8] Mathilde Caron, Hugo Touvron, Ishan Misra, Hervé Jégou, Julien Mairal, Piotr Bojanowski, and Armand Joulin. Emerging properties in self-supervised vision transformers, 2021. 1
- [9] Richard J Chen, Tong Ding, Ming Y Lu, Drew FK Williamson, Guillaume Jaume, Andrew H Song, Bowen Chen, Andrew Zhang, Daniel Shao, Muhammad Shaban, et al. Towards a general-purpose foundation model for computational pathology. *Nature Medicine*, pages 1–13, 2024. 1, 3
- [10] Ting Chen, Simon Kornblith, Mohammad Norouzi, and Geoffrey Hinton. A simple framework for contrastive learning of visual representations, 2020. 1
- [11] Xinlei Chen and Kaiming He. Exploring simple siamese representation learning, 2020. 1
- [12] Ozan Ciga, Tony Xu, and Anne Louise Martel. Self supervised contrastive learning for digital histopathology. *Machine Learning with Applications*, 7:100198, 2022. 1, 2
- [13] Michael Cooper, Zongliang Ji, and Rahul G Krishnan. Machine learning in computational histopathology: Challenges and opportunities. *Genes, Chromosomes and Cancer*, 2023. 1
- [14] Shujian Deng, Xin Zhang, Wen Yan, Eric I-Chao Chang, Yubo Fan, Maode Lai, and Yan Xu. Deep learning in digital

- pathology image analysis: a survey. *Frontiers of medicine*, 14:470–487, 2020. 1
- [15] Jonas Dippel, Barbara Feulner, Tobias Winterhoff, Simon Schallenberg, Gabriel Dernbach, Andreas Kunft, Stephan Tietz, Philipp Jurmeister, David Horst, Lukas Ruff, Klaus-Robert Müller, Frederick Klauschen, and Maximilian Alber. RudolfV: A foundation model by pathologists for pathologists, 2024. 1, 2, 3
- [16] Alexey Dosovitskiy, Lucas Beyer, Alexander Kolesnikov, Dirk Weissenborn, Xiaohua Zhai, Thomas Unterthiner, Mostafa Dehghani, Matthias Minderer, Georg Heigold, Sylvain Gelly, et al. An image is worth 16x16 words: Transformers for image recognition at scale. *arXiv preprint arXiv:2010.11929*, 2020. 2, 4
- [17] Alexandre Filiot, Ridouane Ghermi, Antoine Olivier, Paul Jacob, Lucas Fidon, Alice Mac Kain, Charlie Saillard, and Jean-Baptiste Schiratti. Scaling self-supervised learning for histopathology with masked image modeling. *medRxiv*, pages 2023–07, 2023. 1
- [18] Jean-Bastien Grill, Florian Strub, Florent Altché, Corentin Tallec, Pierre H. Richemond, Elena Buchatskaya, Carl Doersch, Bernardo Avila Pires, Zhaohan Daniel Guo, Mohammad Gheshlaghi Azar, Bilal Piot, Koray Kavukcuoglu, Rémi Munos, and Michal Valko. Bootstrap your own latent: A new approach to self-supervised learning, 2020. 1
- [19] Sai Chowdary Gullapally, Yibo Zhang, Nitin Kumar Mittal, Deeksha Kartik, Sandhya Srinivasan, Kevin Rose, Daniel Shenker, Dinkar Juyal, Harshith Padigela, Raymond Biju, et al. Synthetic domain-targeted augmentation (S-DOTA) improves model generalization in digital pathology. *arXiv preprint arXiv:2305.02401*, 2023. 2
- [20] Lu Han, Han-Jia Ye, and De-Chuan Zhan. Augmentation component analysis: Modeling similarity via the augmentation overlaps. *arXiv preprint arXiv:2206.00471*, 2022. 3
- [21] Kaiming He, Xinlei Chen, Saining Xie, Yanghao Li, Piotr Dollár, and Ross Girshick. Masked autoencoders are scalable vision learners, 2021. 5, 6
- [22] Weiran Huang, Mingyang Yi, Xuyang Zhao, and Zihao Jiang. Towards the generalization of contrastive self-supervised learning. *arXiv preprint arXiv:2111.00743*, 2021. 3
- [23] Mingu Kang, Heon Song, Seonwook Park, Donggeun Yoo, and Sérgio Pereira. Benchmarking self-supervised learning on diverse pathology datasets. In *Proceedings of the IEEE/CVF Conference on Computer Vision and Pattern Recognition*, pages 3344–3354, 2023. 1, 3, 5
- [24] Jakob Nikolas Kather, Niels Halama, and Alexander Marx. 100,000 histological images of human colorectal cancer and healthy tissue. *Zenodo*, 2018. 5
- [25] Maxime Oquab, Timothée Darcet, Théo Moutakanni, Huy Vo, Marc Szafraniec, Vasil Khalidov, Pierre Fernandez, Daniel Haziza, Francisco Massa, Alaaeldin El-Nouby, Mahmoud Assran, Nicolas Ballas, Wojciech Galuba, Russell Howes, Po-Yao Huang, Shang-Wen Li, Ishan Misra, Michael Rabbat, Vasu Sharma, Gabriel Synnaeve, Hu Xu, Hervé Jégou, Julien Mairal, Patrick Labatut, Armand Joulin, and Piotr Bojanowski. Dinov2: Learning robust visual features without supervision, 2024. 2, 4
- [26] Colorado J. Reed, Ritwik Gupta, Shufan Li, Sarah Brockman, Christopher Funk, Brian Clipp, Kurt Keutzer, Salvatore Candido, Matt Uyttendaele, and Trevor Darrell. Scale-mae: A scale-aware masked autoencoder for multiscale geospatial representation learning, 2023. 4
- [27] Alexandre Sablayrolles, Matthijs Douze, Cordelia Schmid, and Hervé Jégou. Spreading vectors for similarity search, 2019. 3
- [28] Andrew H Song, Guillaume Jaume, Drew FK Williamson, Ming Y Lu, Anurag Vaidya, Tiffany R Miller, and Faisal Mahmood. Artificial intelligence for digital and computational pathology. *Nature Reviews Bioengineering*, 1(12): 930–949, 2023. 1
- [29] Chetan L Srinidhi, Ozan Ciga, and Anne L Martel. Deep neural network models for computational histopathology: A survey. *Medical Image Analysis*, 67:101813, 2021. 1
- [30] David Tellez, Geert Litjens, Péter Bándi, Wouter Bulten, John-Melle Bokhorst, Francesco Ciompi, and Jeroen Van Der Laak. Quantifying the effects of data augmentation and stain color normalization in convolutional neural networks for computational pathology. *Medical image analysis*, 58: 101544, 2019. 2
- [31] Bastiaan S Veeling, Jasper Linmans, Jim Winkens, Taco Cohen, and Max Welling. Rotation equivariant cnns for digital pathology. In *Medical Image Computing and Computer Assisted Intervention—MICCAI 2018: 21st International Conference, Granada, Spain, September 16–20, 2018, Proceedings, Part II 11*, pages 210–218. Springer, 2018. 5
- [32] Eugene Vorontsov, Alican Bozkurt, Adam Casson, George Shaikovski, Michal Zelechowski, Siqi Liu, Kristen Severson, Eric Zimmermann, James Hall, Neil Tenenholtz, Nicolo Fusi, Philippe Mathieu, Alexander van Eck, Donghun Lee, Julian Viret, Eric Robert, Yi Kan Wang, Jeremy D. Kunz, Matthew C. H. Lee, Jan Bernhard, Ran A. Godrich, Gerard Oakley, Ewan Millar, Matthew Hanna, Juan Retamero, William A. Moye, Razik Yousfi, Christopher Kanan, David Klimstra, Brandon Rothrock, and Thomas J. Fuchs. Virchow: A million-slide digital pathology foundation model, 2024. 1, 3, 5
- [33] Tongzhou Wang and Phillip Isola. Understanding contrastive representation learning through alignment and uniformity on the hypersphere, 2022. 1, 4
- [34] Xiyue Wang, Sen Yang, Jun Zhang, Minghui Wang, Jing Zhang, Wei Yang, Junzhou Huang, and Xiao Han. Transformer-based unsupervised contrastive learning for histopathological image classification. *Medical image analysis*, 81:102559, 2022. 1, 2
- [35] Jerry Wei, Arief Suriawinata, Bing Ren, Xiaoying Liu, Mikhail Lisovsky, Louis Vaickus, Charles Brown, Michael Baker, Naofumi Tomita, Lorenzo Torresani, et al. A petri dish for histopathology image analysis. In *Artificial Intelligence in Medicine: 19th International Conference on Artificial Intelligence in Medicine, AIME 2021, Virtual Event, June 15–18, 2021, Proceedings*, pages 11–24. Springer, 2021. 5
- [36] Chun-Hsiao Yeh, Cheng-Yao Hong, Yen-Chi Hsu, Tyng-Luh Liu, Yubei Chen, and Yann LeCun. Decoupled contrastive learning, 2022. 4

- [37] Jure Zbontar, Li Jing, Ishan Misra, Yann LeCun, and Stéphane Deny. Barlow twins: Self-supervised learning via redundancy reduction, 2021. [1](#)

A. Extended-Context Translation

ECT is simply implemented using native crop-and-resize torchvision transformation operations by selecting appropriate scale and aspect ratio parameters. The augmentation can be used as a drop in replacement into any pipeline that may accommodate the change in input tile sizes. Proper behavior assumes the input size is greater than the output size.

```
class RandomExtendedContextTranslation(RandomResizedCrop):
    def __init__(
        self,
        input_size: int,
        output_size: int,
        scale: Tuple[float, float],
        ratio: Tuple[float, float]
    ) -> None:

        # change in area
        min_scale, max_scale = scale
        adjustment = (output_size / input_size)**2
        adjusted_scale = (min_scale * adjustment, max_scale * adjustment)

        # override base class with adjustment
        super(RandomExtendedContextTranslation, self).__init__(
            size=output_size,
            scale=adjusted_scale,
            ratio=ratio
        )
```

Figure 3. Translation behavior is controlled with a smaller aspect ratio and adjusted scale range computed using ratio of patch area.

Global crops select an input size of 392 and an output size of 224 with a scale range of [0.9, 1.1] applied on the target output size. The adjustment factor computed as the ratio of areas, $(\frac{224}{392})^2$, that is multiplied with the scale range to account for the change in input size and output size. The same logic is applied to local crops, while aspect ratios are held fixed with ranges of [0.95, 1.05] to ensure minimal distortion.